16th World Conference on Earthquake, 16WCEE 2017

Santiago Chile, January 9th to 13th 2017

Paper N° 4525

Registration Code: S- Q1464334221

AMBIENT SEISMIC NOISE TOMOGRAPHY OF SANTIAGO BASIN: PRELIMINARY RESULTS

J.Salomón[1], M. Sáez[2], C. Pastén[3] ,S.Ruiz[4] ,F. Leyton[5] F. Ortega[6]

[1] *Department of Civil Engineering, University of Chile, Santiago, Chile, jose.salomon@ing.uchile.cl*
[2] *Department of Civil Engineering, University of Chile, Santiago, Chile, misaez@ing.uchile.cl*
[3] *Department of Civil Engineering, University of Chile, Santiago, Chile, cpasten@ing.uchile.cl*
[4] *Department of Geophysics, University of Chile, Santiago, Chile, sruiz@dgf.uchile.cl*
[5] *National Seismological Center, University of Chile, Santiago, Chile, leyton@csn.uchile.cl*
[6] *Department of Geophysics, University of Chile, Santiago, Chile, ortega@dgf.uchile.cl*

Abstract

Evaluation of the seismic site response of the Santiago Basin requires a detailed shear wave velocity model that accounts for vertical variations in relatively short distances. A temporal broadband station network was deployed in the center of the Basin and continuously recorded months of seismic ambient noise. The vertical components of the records were used to calculate empirical Green's functions from noise cross-correlation. Frequency-domain cross-correlations were calculated based on Aki's (1957) formulation. Identification of zero-crossings in the real part of the cross spectrum, the cross-correlation function in the frequency domain, were associated with the Bessel function's zeros to obtain phase-velocity dispersion curves. Phase velocity maps for periods ranging from 1 to 3 s were constructed with phase dispersion curves using a regularized weighted least squares tomographic method. For this purpose, the study area was divided into a geographical grid with size 2x2 km. We concluded that the obtained velocity maps show that the south of the basin has larger velocities compared to the north zone, which is consistent with previous studies. The results are also consistent with the main geological boundaries of the basin (San Cristobal Hill, the Chena Hill, and the western flank of the Andes) and available large-scale velocity models.

Keywords: Tomography, ambient noise cross-correlation, shear wave velocity, seismic characterization, dispersion curve.

1.Introduction

In the last decades, two mega earthquakes have struck the Santiago basin: the 1985 Mw 8.0 Valparaiso and the 2010 Mw 8.8 Maule earthquakes, both of which generated significant social and economic damage (Astroza et al. 2012). The observed damage intensities during these earthquakes were ranged between VI and VIII and were mainly associated to surface geology (Leyton et al., 2011; Astroza et al., 2012). Given the fact that the Santiago basin host more than half of the Chilean population, it is necessary to understand its seismic response.

The dynamic seismic response of Santiago basin has been studied by different authors. Pilz et al. (2010), using the H/V spectral ratio method and gravimetric measurements from Araneda et al. (2000), proposed a shear wave velocity model covering a small area of the northern part of the basin, characterized by clear peaked H/V curves. On the other hand, Toledo (2008) performed a numerical model of the seismic response of the basin using spectral elements, but he couldn't reach conclusive results mainly due to the simple shear wave velocity model adopted. Recently, Pasten et al. (2016) did a deep characterization of the Santiago basin using HVSR and cross-correlation of ambient noise.

The methodology used by Pasten et al. (2016) has been promoted in the last years, different researchers (Shapiro and Campillo 2004, Sabra et al. 2005, Roux et al. 2005) have shown that the cross-correlation of long time series of seismic noise converge to their Green's function between two sensors, allowing to estimate the dispersive characteristics of the medium (dispersion curves). The cross-correlation of seismic noise has been used in different scales and frequency ranges, making possible the generation of velocity maps for different periods that, in turn, are used to determinate the velocity structure of the medium, a technique denominated Ambient Noise Tomography (ANT) (Bensen et al. 2009, Yang et al. 2009, and Ward et al. 2013).

In this study, we deployed a set of broadband stations that recorded ambient noise continuously for several months (see Fig. 1). The vertical components of the record were cross-correlated in order to compute phase velocity dispersion curves for different sectors in the basin, in a wide frequency range. These dispersion curves were used to generate phase velocity maps of the Santiago basin at frequencies ranging between 0.3 y 0.9 Hz which were correlated with the main rock outcrops.

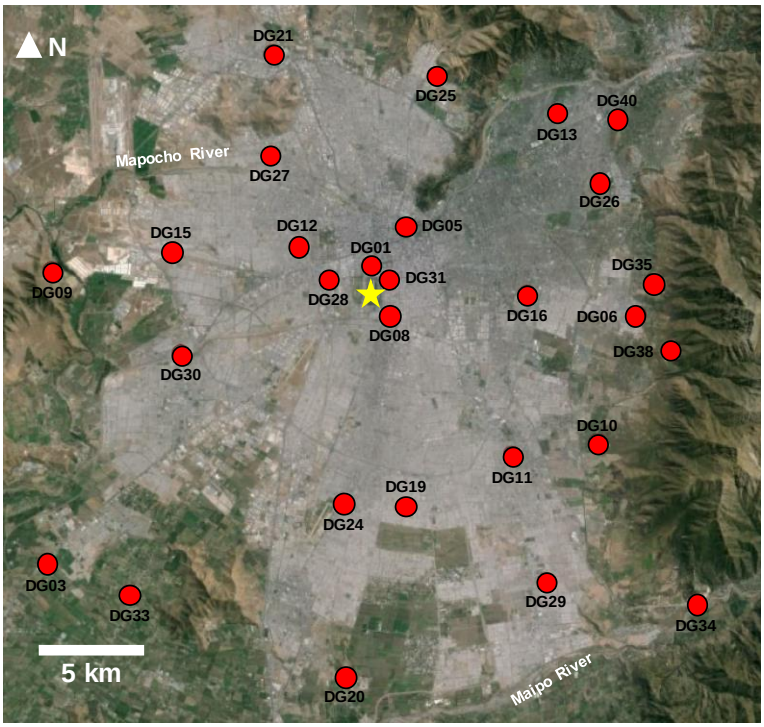

Fig. 1- Google Earth map showing location of the 31 broadband stations (red circles) used in this study, labels show the station code. The yellow star represents the position of a local experiment, see text for details.

2. Data Processing

Thirty one broadband stations deployed in different sites in the Santiago basin recorded months of ambient seismic noise data [see Fig. (1)]. Every station was equipped with a broadband Trillium compact 120 sec-period sensor, a 24-bit Quanterra Q330 digitizer, a Marmot data logger system and a GPS antenna. The stations recorded in continuously in time the three components at a rate of 100 samples per second from July 2013 to March 2014.

In order to extract the Green's functions between receivers, we calculated the cross-correlation of the vertical component of the records following the spectral methodology proposed by Pasten et al. (2016). The aim of the methodology is to calculate phase velocity using a method based on the SPAC method, developed by Aki (1957) with some modification that attempts to improve the high frequency range. The methodology follows these steps:

(i) The raw data are high-pass filtered with a fourth-order filter of cutoff frequency at 0.01 Hz, and divided in two-minutes windows.

(ii) The cross-correlation spectrum is calculated in each window.

(iii) The real component of the cross spectrum is normalized by the maximum absolute value and is stacked daily (Fig. 2a). The daily real-spectrum is stacked generating the final spectrum.

(iv) The final spectrum is plotted as a function of frequency, and the zero-crossing frequencies are identified (Fig. 2b) and associated to the zero-crossings of the zero-order Bessel function of the first kind.

(v) The phase velocity $c(f_n)$ is calculated from the interstation distance Δ, and the value of the zero crossing frequency of the Bessel function z_{n+m} (Fig.2c) as:

$$c(f_n) = \frac{2\pi f_n \Delta}{z_{n+m}} \tag{1}$$

where m indicates the missing or extra zero crossings (Ekström, 2009). Eq. (1) generates a family of dispersion curves depending on the selected m. We chose the m-value such that the resulting velocity curve falls within a realistic range of the expected phase velocities.

We calculated more than four hundred correlations, which were calculated using an automatic selection criterion based on the stability of the daily spectrum at each frequency. To apply the criterion, we normalized the daily spectrum using a one-bit normalization (Fig. 3a): all the positive amplitudes of the real part of the cross spectrum are set to 1 and the negative ones to -1. Then, the amplitudes are stacked generating the "one-bit" final spectrum (Fig. 3b). This normalization generates a cross-spectrum with amplitudes close to +/- 1 when the daily spectra are consistent over time. Finally, we calculated the standard deviation at each frequency; if the daily spectrum at a given frequency is stable, the standard deviation is close to zero. We found that frequencies with standard deviations lower than 0.8 are associated to zero-crossings that can be clearly identified, when the curve is smoothed over a 0.2 Hz bandwidth (Fig. 3c).

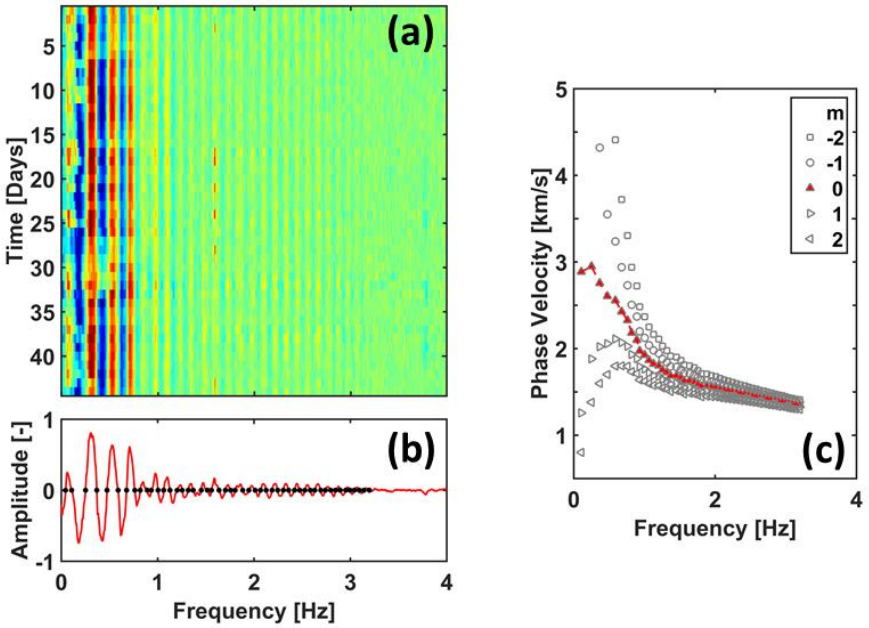

Fig. 2 - Phase velocity methodology: (a) Color map of real component of the cross spectrum after daily stacking 2 min windows, (b) stacked daily cross-spectrum, and (c) dispersion curves calculated with Eq. (1) for different m-value. Red triangles indicate the selected dispersion curve.

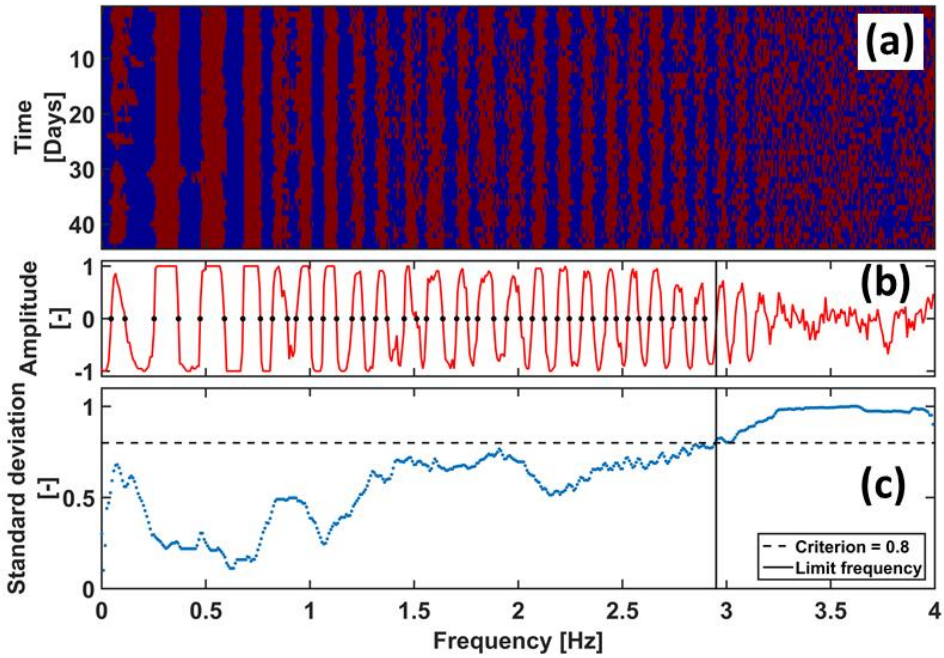

Fig. 3- Automatic selection criterion. (a) Color map of real component of the cross spectrum normalized with one bit after daily stacking of 2 min windows, (b) final stacked cross-spectrum (c) standard deviation of the cross-spectrum at each frequency smoothed over a 0.2Hz bandwidth.

The adopted methodology and selection criterion enable us to successfully calculate 288 phase velocity dispersion curves (Fig. 4) out of the total 402 in a frequency range between 0.1 and 4 Hz.

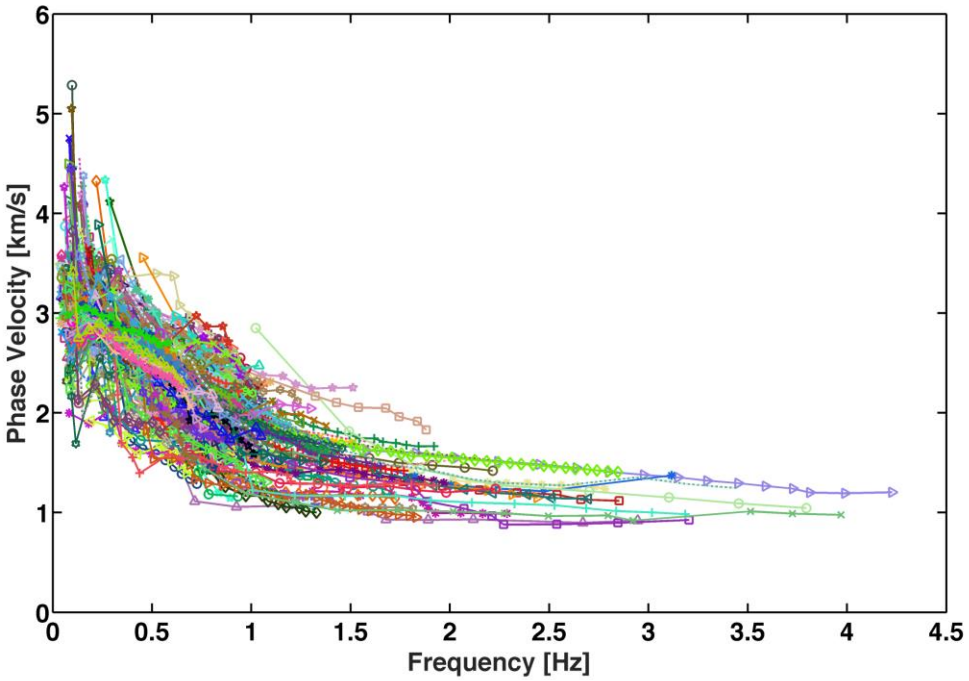

Fig. 4 - Selected phase velocity dispersion curves.

3. Inversion Scheme

The Rayleigh wave traveltime *t* between two stations (at certain frequency *f*) can be obtained relating it to a slowness field *s(f)* (inverse of velocity) through a propagation path *l(s)* according to the following expression:

$$t = \oint_L s \, dl \tag{2}$$

This equation corresponds to a Fredholm integral of the first kind, whose computation is inherently nonlinear due to the dependency of the wave propagation path on the velocity (or slowness) structure of the media. However, a linear approximation of Eq. (2) is widely used in this kind of problems (Picozzi et al. 2009, Hannemann et al. 2014, Pilz et al. 2012). On the other hand, Kugler et al. (2007) proposed that, given the error levels associated to the data in tomographic studies from shallow surveys, a linear approximation based on straight ray paths has no significant impact on the estimated slowness model. Moreover, the forward problem can be written in a linear form discretizing the slowness field in a 2D array conformed by a total of M pixels in which slowness is assumed to be constant. Then, Eq. (1) becomes

$$\underline{t} = \underline{\underline{G}}\,\underline{s} \tag{3}$$

where $\underline{t}$ is the travel time vector [Nx1], $\underline{s}$ is the slowness vector [Mx1], and $\underline{\underline{G}}$ is the design matrix [NxM] or data kernel, where each row is associated to a ray of the experiment and the non zero elements contains the length of such ray that passes through the corresponding pixel of the slowness model.

Usually, having a forward model like the Fredholm integral (2) results in an ill posed estimation problem, where the design matrix G is not invertible, making it impossible to estimate $\underline{s}$ from Eq. (3) directly. As a first approach, the problem could be solved minimizing the error norm between the observed t_{obs} and predicted *t* travel time vectors alone. However, most tomographic problems can be considered as a mixed or

underdetermined linear system, so the solution requires a priori information about the estimated model. We add a priori information by introducing a regularization term in which we search for tomography models that are smooth. (e.g., Menke 2012). A discrete Laplacian matrix ∇^2 is widely used as regularizing operator assuming a spatially smooth varying slowness field (Sasaki, 1992). Then, the slowness field $\underline{s}$ can be estimated by minimizing the misfit function ϕ,

$$\phi(\underline{s}) = (\underline{t} - \underline{\underline{G}}\underline{s})^T (\underline{t} - \underline{\underline{G}}\underline{s}) + \varepsilon^2 \left[\nabla^2 (\underline{s} - \underline{s}_o)\right] \tag{4}$$

where $\underline{s}_o$ is an *a priori* slowness model and ε^2 is the damping parameter that represents the weight assigned to the a priori information. Therefore, for each value of the damping parameter we obtain slowness estimates by minimizing the misfit function. In order to obtain the optimal value of ε^2, we use the generalized cross validation method (Craven & Wahba 1979), in which the best value of ε^2 is selected using a criterion based on the data. The ordinary or "leave-one-out" cross validation method considers the estimated models that are obtained by leaving one of the N data points out of the fitting process for different values of the damping parameter and then choosing the optimal damped parameter as the one associated to the model that better predict the data that is left out of the inversion process (Aster 2005). The method refers to find a value of ε^2 that minimizes the cross validation function $g(\varepsilon^2)$ estimated by

$$g(\varepsilon^2) = \frac{1}{N} \sum_{k=1}^{N} \left[\frac{\underline{\underline{G}}\underline{s}_k - \underline{t}_k}{1 - \underline{\underline{G}}\underline{\underline{G}}^{-g}} \right]^2 \tag{5}$$

where $\underline{\underline{I}}$ is an MxM identity matrix and $\underline{\underline{G}}^{-g}$ is the generalized inverse for the regularized problem (Aster 2005).

The observed traveltime t_{obs} for each pair of stations is obtained from the phase velocity dispersion curves calculated in data processing according to the expression

$$t_{obs} = \frac{l_{st}}{c} \tag{6}$$

where l_{st} is the ray length between stations.

4. Mesh Definition

4.1 Path coverage and frequencies definition

In order to define the frequency range for the noise tomography, the path coverage in the basin is analyzed in relation to frequency. For each pair of stations, we determined the maximum valid frequency as the one defined by the standard deviation criterion previously explained and a minimum valid frequency determined from the interstation distance as the maximum wavelength (Luo et. al 2015).

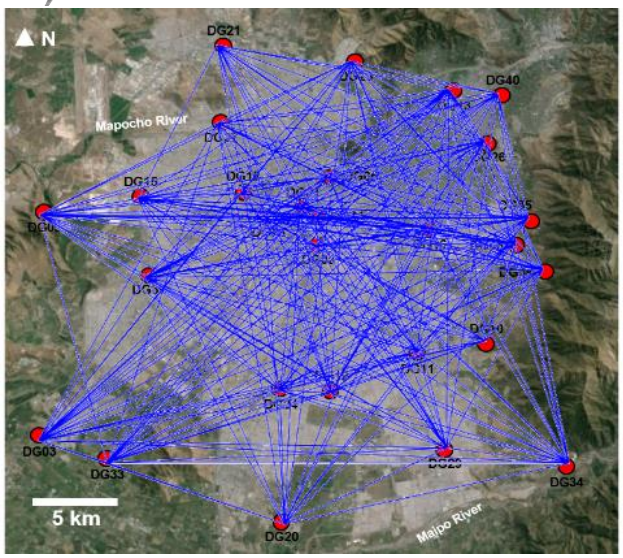

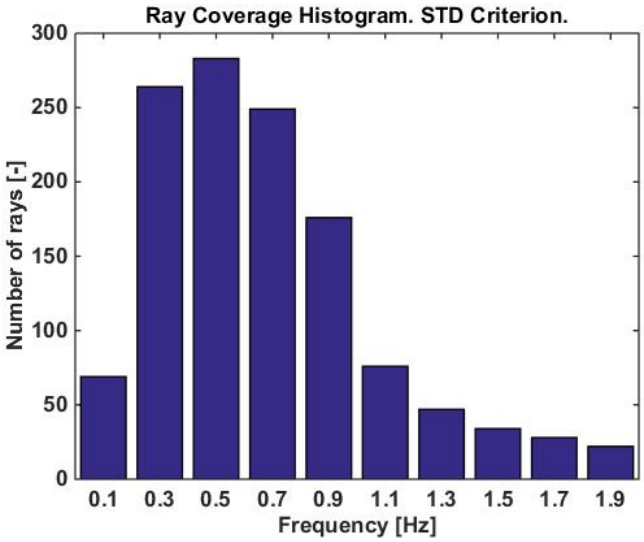

Fig. 5 - (a) Path coverage rays at 0.5 Hz (b) Frequencies histogram.

The path-frequency analysis shows that the best ray coverage is found at 0.5 Hz (Fig.5a), spanning most of the 2D structure site. Similarly, the frequency histogram shown in Fig.5b indicates an adequate coverage up to 0.9 Hz. Then, adopting at least 150 rays crossing most of the basin geometry, the frequency range of interest is from 0.3 Hz to 0.9 Hz.

4.2 Model discretization

The spatial discretization and resolution of the slowness field is constrained by the larger wavelength observed at each frequency. The quarter-wavelength criterion has been used by several authors as the model resolution limit (Long and Kocaoglu 2001), and establishes that the deviation of the wave paths from a straight line in media with slight velocity anomalies is either of the same order of the pixels dimension or less than a quarter of the wavelength (Pilz et.al 2012). Then, as an average, the model is discretized into 2x2 km^2 pixels, covering an area of 32x30 km^2.

5. Data Validation

We performed a checkerboard test with a synthetic velocity model to evaluate the quality of the ray path coverage (for each frequency) and to verify its capability to detect high velocity contrasts. The generated checkerboard alternates velocity zones of 1000 m/s and 2000 m/s (a velocity contrast of a 100%).

The checkerboard model is used to generate synthetic travel time data $\underline{t}_{syn}$, usually disturbed by adding a Gaussian distributed noise $\underline{n}$ (Loris et. al 2010), with zero mean and a variance of 5% of the data. Considering the ray coverage at each frequency, the synthetic travel times are:

$$\underline{t}_{syn} = \underline{\underline{G}}\,\underline{s}_{syn} + \underline{n} \tag{7}$$

The inversion is performed following the procedure explained in Section 3. We considered the mean value of the checkerboard as the *a priori* slowness model $\underline{s}_o$.

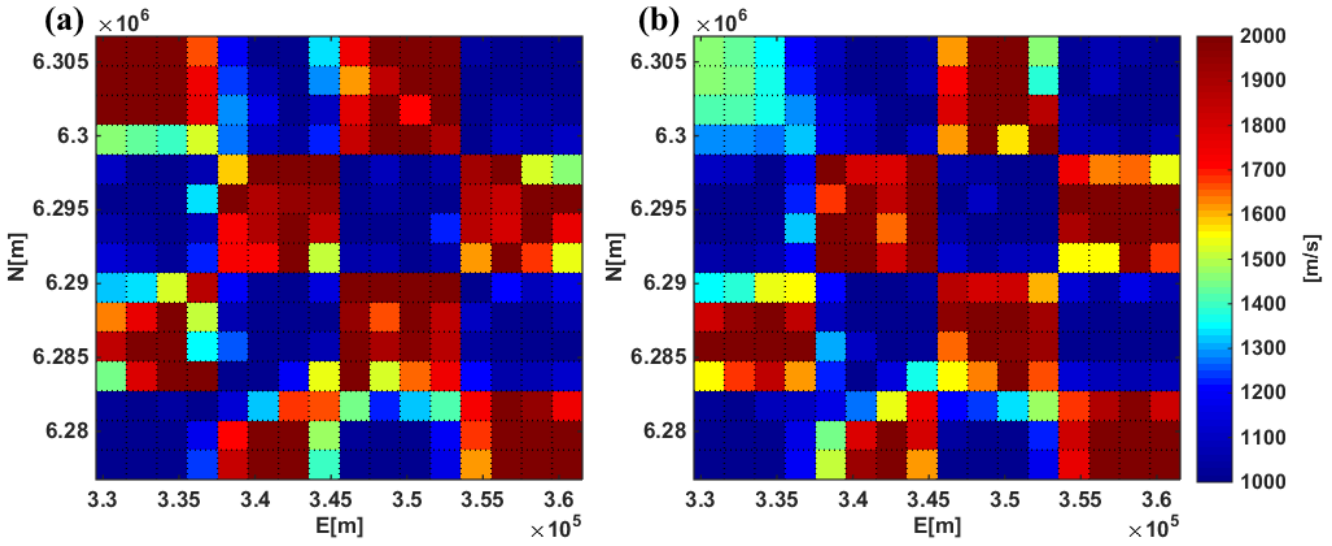

Fig.6 -Estimated synthetic models at (a) 0.3 Hz and (b) 0.6 Hz.

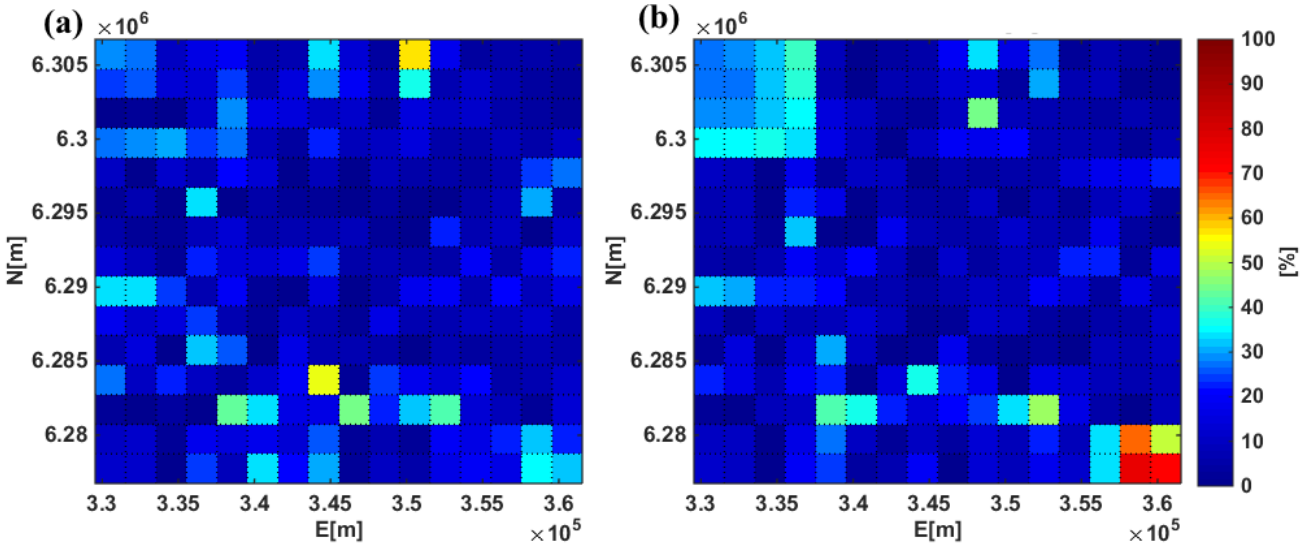

Fig. 7 - Estimated errors at (a) 0.3 Hz and (b) 0.6 Hz.

Comparing the initial model and the estimated ones in Fig. 6 we can see that the synthetic structure is well reproduced for the selected frequencies, except in the northwest zone where the ray density is lower than average. This assessment is confirmed by the percentage error between the models as shown in Fig.7a and 7b, with a mean error of 12.9% and 15.2%, respectively. These results suggest that the available ray coverage could be appropriate to capture the real velocity model.

6. Results

The velocity maps derived from the inversion process are shown in Fig. 8. The results are expressed in terms of the perturbation percentage regarding to the average map velocity value. Note that the pixels with zero ray crossing are painted in gray.

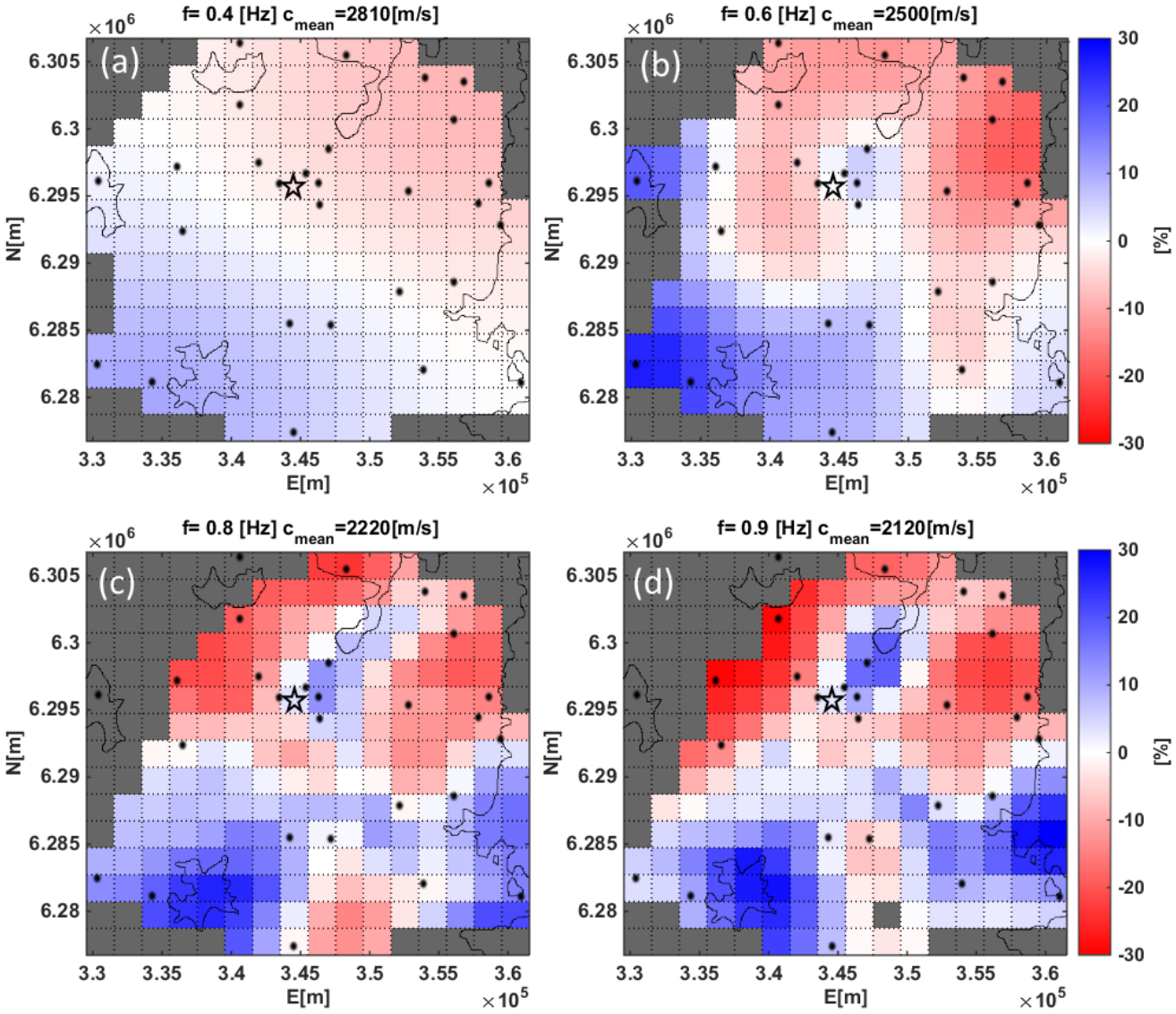

Fig. 8 -Phase velocity maps at (a) 0.4 Hz (b) 0.6 Hz (c) 0.8 Hz (d) 0.9 Hz. Black star represents the position of local experiment, see text for details. Black dots indicate the position of the broadband stations.

7. Discussion

The estimated velocity maps (Fig. 8) show perturbation values up to 30% of the average velocity, being smaller at lower frequencies. This velocity distribution can be associated to an increasing heterogeneity at higher frequencies (shallower depths). Also, the high velocity zones shown in Fig. 8c and Fig. 8d are in good agreement with the main rock outcrops in the Basin: the San Cristobal Hill, the Chena Hill, and the western flank of the Andes.

An important aspect of the velocity model is its resolution with depth. Urban (1993) and Panza (1981) proposed that the fundamental mode of a Rayleigh wave exhibits its maximum sensitivity at depths between a third and a half of the maximum wavelength. Therefore, according to the average map velocity values, the depth sensitivity of the model is approximately restricted to ~4.7 km depth at 0.3 Hz (for a ~9.5 km wavelength) and ~1.2 km depth at 0.9 Hz (for a ~2.4 km wavelength).

Using gravimetric data, Yañez et.al (2015) defined that the quaternary sedimentary cover of the Santiago basin has 250 m of average depth and three depocenters that reach approximately 600 m, which cannot be solved in the frequency range solved in this study. The results we found are more likely related to deeper geological structures. At regional scale, the shallower quaternary deposits are above the Abanico Formation (Gambiagi et. al 2014), which consists of volcanic and sedimentary sequences deposited during Oligocene/Early Miocene, and built by volcaniclastic rocks, tuffs, basic lavas, ignimbrites and different sediments (Charrier et al. 2002). The Abanico Formation has a variable thickness along the West Andean Thrust, reaching an exposed one of approximately ~4 km (Armijo et al. 2010).

Farías et al. (2010) developed a crustal-scale shear wave velocity model for the Andes of Central Chile using seismological and geological data. S-wave velocities of ~3000-3200 m/s varies from the sea level up to 5 km depth, which are associated to the Abanico Formation. Aiming for engineering purposes, these velocity values v_s can be expressed in terms of phase velocity c as

$$c = k\, v_s \tag{8}$$

where *k* is a constant value limited between 0.9 and 0.95 for typical values of Poisson's ratio (from 0.2 up to 0.4) (Pilz el al. 2012). Then, the crustal model phase velocity values (~2850-3050 m/s) are similar to the obtained low frequency average values (~2990 m/s at 0.3 Hz and ~2810 m/s at 0.4 Hz), where the influence of shallow heterogeneities are negligible.

As a complement of the tomographic results, we performed a small-scale experiment at Parque O'Higgins in the center of the basin (yellow star in Fig. 8). We deployed two linear arrays spaced at 60 m and 30 m .We further complemented the intermediate frequency range using a single pair of broadband stations (DG28 and DG31) spaced at 2.9 km. As shown in Fig. 9 the tomographic results have a good agreement with the intermediate and local dispersion curves. This example shows how to complement data from local arrays to improve the definition of dispersion curves at lower frequencies and, hence, the inversion of deeper shear wave velocity profiles.

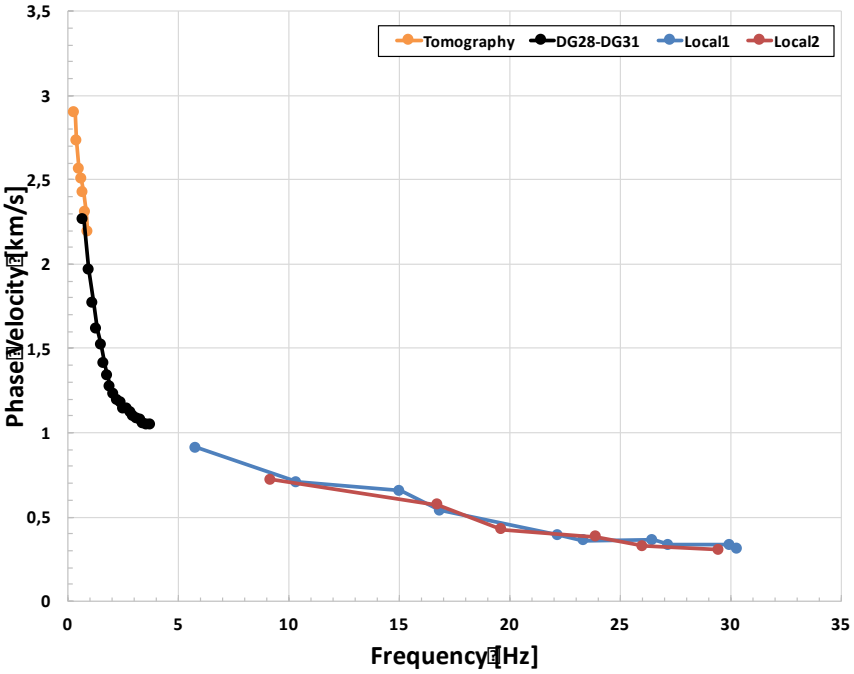

Fig. 9 -Phase velocity dispersion curve in a wide frequency range, using tomography results (orange line), dispersion curve between DG28-DG31 (black line) and local campaing (red and blue line).

8. Conclusions

The ambient noise cross-correlation is a useful tool to calculate dispersion curves in a wide range of frequencies, allowing us to characterize deep and shallow geological structures depending on the distance between receivers.

We computed over 300 dispersion curves from the real component of the cross-correlation of ambient seismic noise records in order to get phase velocity maps along a frequency range between 0.3-0.9 Hz. The velocity maps were obtained using an inversion technique validated through checkerboard tests. The validation shows that the ray coverage ensures a good recovery of the initial model, except in the northwest zone where the ray density is sparse.

The obtained velocity maps show that the south of the basin has larger velocities compared to the north zone, which is consistent with Pastén et al. (2016). The results are also consistent with the main geological boundaries of the basin (high frequencies) and available large-scale velocity models (low frequencies).

The implemented methodology allows estimating velocity models that will allow the numerical modeling of the basin dynamic behavior. In order to improve the resolution and the frequency range of the model, we suggest to complement the data with local passive arrays focusing on low ray density areas, including short and intermediate distance, such as the northwestern part of the Basin.

9. Acknowledgments

We would like to thank the National Seismological Center for allowing us to deploy the instruments in the Santiago Basin.

10. References

[1] Aki, K. (1957) Space and time spectra of stationary stochastic waves, with special reference to microtremors. *Bulletin of Earthquake Engineering* 35:415-456.

[2] Astroza, M., Ruiz, S., Astroza, R., 2012. Damage assessment and seismic intensity analysis of the 2010 (Mw 8.8) Maule earthquake. *Earthquake Spectra* 28 (S1), S145–S164.

[3] Leyton, F., Sepúlveda, S.A., Astroza, M., Rebolledo, S., Acevedo, P., Ruiz, S., Gonzalez, L., Foncea, C., 2011. Seismic zonation of the Santiago Basin, Chile. Proceedings of Fifth International Conference on Earthquake Geotechnical Engineering.

[4] Pilz, M., Parolai, S., Picozzi, M., Wang, R., Leyton, F., Campos, J., & Zschau, J. (2010). Shear wave velocity model of the Santiago de Chile basin derived from ambient noise measurements: a comparison of proxies for seismic site conditions and amplification. *Geophysical Journal International,* 182(1), 355-367.

[5] Araneda, M., Avendano, F. & Merlo, C., 2000. Gravity model of the basin in Santiago, Stage III, Proceedings *of the 9th Chilenian Geological Congress*, 2, 404–408.

[6] Toledo, A. (2008) Sobre los estados resonantes de la cuenca de Santiago. *In Departamento de Ingenieria Civil. Universidad de Chile, Santiago, Chile, vol. Tesis para optar al grado de Magíster en Ciencias Mención Geofísica.*

[7] Pastén, C., Sáez, M., Ruiz, S., Leyton, F., Salomón, J. & Poli, P. (2016) Deep characterization of the Santiago Basin using HVSR and cross-correlation of ambient seismic noise. *Engineering Geology.* 201:57-66.

[8] Shapiro, N. M. & Campillo, M. (2004) Emergence of broadband Rayleigh waves from correlations of the ambient seismic noise. *Geophysical Research Letters* 31(7).

[9] Sabra, K. G. (2005) Extracting time-domain Green's function estimates from ambient seismic noise. *Geophysical Research Letters* 32(3).

[10] Roux, P., Sabra, K. G., Kuperman, W. A. & Roux, A. (2005) Ambient noise cross correlation in free space: Theoretical approach. *The Journal of the Acoustical Society of America* 117(1):79.

[11] Bensen, G. D., Ritzwoller, M. H., & Yang, Y. (2009). A 3-D shear velocity model of the crust and uppermost mantle beneath the United States from ambient seismic noise. *Geophysical Journal International*, 177(3), 1177-1196.

[12] Yang, Y., Ritzwoller, M. H., Lin, F. C., Moschetti, M. P., & Shapiro, N. M. (2008). Structure of the crust and uppermost mantle beneath the western United States revealed by ambient noise and earthquake tomography. *Journal of Geophysical Research: Solid Earth*, 113(B12).

[13] Ward, K. M., Porter, R. C., Zandt, G., Beck, S. L., Wagner, L. S., Minaya, E., & Tavera, H. (2013). Ambient noise tomography across the Central Andes. *Geophysical Journal International*, *ggt166*

[14] Ekström, G., Abers, G. A. & Webb, S. C. (2009) Determination of surface-wave phase velocities across USArray from noise and Aki's spectral formulation. *Geophysical Research Letters* 36(18).

[15] Picozzi, M., Parolai, S., Bindi, D., & Strollo, A. (2009). Characterization of shallow geology by high-frequency seismic noise tomography. *Geophysical Journal International*, 176(1), 164-174.

[16] Hannemann, K., Papazachos, C., Ohrnberger, M., Savvaidis, A., Anthymidis, M., & Lontsi, A. M. (2014). Three-dimensional shallow structure from high-frequency ambient noise tomography: New results for the Mygdonia basin-Euroseistest area, northern Greece. *Journal of Geophysical Research: Solid Earth*, 119(6), 4979-4999.

[17] Pilz, M., Parolai, S., Picozzi, M., & Bindi, D. (2012). Three-dimensional shear wave velocity imaging by ambient seismic noise tomography. *Geophysical Journal International*, 189(1), 501-512.

[18] Kugler, S., Bohlen, T., Forbriger, T., Bussat, S., & Klein, G. (2007). Scholte-wave tomography for shallow-water marine sediments. *Geophysical Journal International*, 168(2), 551-570.

[19] Menke, W. (2012). Geophysical data analysis: discrete inverse theory. *Academic press.*

[20] Sasaki, Y. (1992). Resolution of resistivity tomography inferred from numerical simulation. *Geophysical Prospecting*. 40(4), 453-464.

[21] Craven, P., & Wahba, G. (1978). Smoothing noisy data with spline functions. *Numerische Mathematik*, 31(4), 377-403.

[22] Aster, R. C., Borchers, B., & Thurber, C. H. (2011). Parameter estimation and inverse problems. *Academic Press*.

[23] Luo, Y., Yang, Y., Xu, Y., Xu, H., Zhao, K., Wang, K., (2015). On the limitations of interstation distances in ambient noise tomography. *Geophysical Journal International.* 201(2), 652–661.

[24] Long, L. T., & Kocaoglu, A. H. (2001). Surface-wave group-velocity tomography for shallow structures. *Journal of Environmental & Engineering Geophysics*, 6(2), 71-81.

[25] Loris, I., Douma, H., Nolet, G., Daubechies, I., & Regone, C. (2010). Nonlinear regularization techniques for seismic tomography. *Journal of Computational Physics*, 229(3), 890-905.

[26] Urban, L., Cichowicz, A., & Vaccari, F. (1993). Computation of analytical partial derivatives of phase and group velocities for Rayleigh waves with respect to structural parameters. *Studia geophysica et geodaetica*, 37(1), 14-36.

[27] Panza, G. F. (1981). The resolving power of seismic surface waves with respect to crust and upper mantle structural models. *In The solution of the inverse problem in geophysical interpretation (pp. 39-77). Springer US.*

[28] Giambiagi, L., Tassara, A., Mescua, J., Tunik, M., Alvarez, P. P., Godoy, E., & Tapia, F. (2015). Evolution of shallow and deep structures along the Maipo–Tunuyán transect (33° 40′ S): from the Pacific coast to the Andean foreland. *Geological Society, London, Special Publications,* 399(1), 63-82.

[29] Charrier, R., Baeza, O., Elgueta, S., Flynn, J.J., Gans, P., Kay, S.M., Muñoz, N., Wyss, A.R., Zurita, E., (2002). Evidence for cenozoic extensional basin development and tectonic inversion south of the flat-slab segment, southern central andes, Chile (33°-36°S.L.). *J. S. Am. Earth Sci.* 15 (1), 117–139.

[30] Armijo, R., Rauld, R., Thiele, R., Vargas, G., Campos, J., Lacassin, R., Kausel, E., (2010). The west andean thrust, the San ramón fault, and the seismic hazard for Santiago, Chile. *Tectonics* 29 (4), 1–34.

[31] Farías, M., Comte, D., Charrier, R., Martinod, J., David, C., Tassara, A., & Fock, A. (2010). Crustal-scale structural architecture in central Chile based on seismicity and surface geology: Implications for Andean mountain building. *Tectonics*, 29(3).